Journal of Materials Chemistry A

Materials Design of Sodium Chloride Solid Electrolytes Na3MCl6 for All-Solid-State Sodium-Ion Batteries

Journal:	*Journal of Materials Chemistry A*
Manuscript ID	TA-ART-08-2021-007050.R1
Article Type:	Paper
Date Submitted by the Author:	09-Sep-2021
Complete List of Authors:	Park, Dongsu; Korea Institute of Science and Technology, Kim, Kwangnam; Lawrence Livermore National Laboratory Chun, Gin Hyung; Korea Institute of Science and Technology, Center for Energy Storage Research Wood, Brandon; Lawrence Livermore National Laboratory Shim, Joon Hyung; Korea University, Mechanical Engineering Yu, Seungho; Korea Institute of Science and Technology, Center for Energy Storage Research

ARTICLE

Materials Design of Sodium Chloride Solid Electrolytes Na_3MCl_6 for All-Solid-State Sodium-Ion Batteries

Received 00th January 20xx,
Accepted 00th January 20xx

DOI: 10.1039/x0xx00000x

Dongsu Park,[a,b] Kwangnam Kim,[c] Gin Hyung Chun,[a,b] Brandon C. Wood,[c] Joon Hyung Shim,[b,*] and Seungho Yu[a,d,*]

All-solid-state sodium-ion batteries have attracted increasing attention owing to the low cost of sodium and the enhanced safety compared to conventional Li-ion batteries. Recently, halides have been considered as promising solid electrolytes (SEs) due to their favorable combination of high ionic conductivity and chemical stability against high-voltage cathode materials. Although a wide variety of lithium chloride SEs, Li_3MCl_6, have been developed for high-voltage all-solid-state batteries, only a limited number of sodium chloride SEs have been reported. This study aims to offer a material design insight for the development of sodium chloride SEs through systematic assessment of the phase stability, electrochemical stability, and transport properties of novel Na_3MCl_6 SEs. Structural calculations indicate that Na_3MCl_6 exhibits trigonal $P\bar{3}1c$, monoclinic $P2_1/n$, and trigonal $R\bar{3}$ phases, and the stable phase of Na_3MCl_6 is dependent on the type and ionic radius of M. Na_3MCl_6 typically exhibits a high oxidation potential, demonstrating good electrochemical stability against cathodes. The bond-valence site energy and *ab initio* molecular dynamics calculations revealed that Na_3MCl_6 with $P2_1/n$ and $R\bar{3}$ phases showed low ionic conductivity, whereas the $P\bar{3}1c$ phase slightly improved the ionic conductivity of Na_3MCl_6. The formation of Na vacancies by aliovalent substitution considerably increased the ionic conductivity up to four orders of magnitude for pristine Na_3MCl_6, exhibiting ~10^{-5} S/cm for trigonal $P\bar{3}1c$ and $R\bar{3}$ phases, which is comparable to the highest ionic conductivity among the reported Na chloride SEs. The formation of defects could further enhance the ionic conductivity of Na_3MCl_6, and the optimization of defect type and ratio can be helpful in developing superionic Na chloride SEs. The material design of Na_3MCl_6 in this study will be fundamental guidelines for the development of novel sodium halide SEs for all-solid-state sodium-ion batteries.

Introduction

The development of next-generation batteries has been widely conducted for emerging applications such as energy storage systems (ESSs) and electric vehicles.[1] All-solid-state batteries (ASSBs) are promising candidates for next-generation batteries owing to their high energy density and enhanced safety.[2] Solid electrolytes (SEs) in ASSBs enable the use of metallic anodes exhibiting higher energy density than graphite anodes. SEs also significantly enhance safety by replacing flammable organic liquid electrolytes in conventional Li-ion batteries.[3] Recently, ASSBs employing Na-ion SEs have been considered due to the low cost of sodium and enhanced safety compared to conventional Li-ion batteries.[4, 5] The abundance of sodium particularly facilitated the development of low-cost batteries for large-scale applications such as ESS.[6]

Among the various types of Na-ion SEs, sulfide SEs have been widely investigated owing to their high ionic conductivities.[7-11] For example, Na_3PS_4, Na_3SbS_4, and $Na_{11}Sn_2PS_{12}$ exhibited conductivities of 0.1–10 mS/cm,[7-10] and W-substituted Na_3SbS_4 showed a high conductivity of 41 mS/cm.[9, 12] However, sulfide SEs exhibit a narrow electrochemical stability window, resulting in poor compatibility with metal anodes and typical cathode materials.[13, 14] In addition, phosphorus-based sulfide SEs are unstable against humid air and are prone to generate toxic H_2S gas.[15, 16] Oxide SEs such as NASICONs and *β*-alumina exhibit good chemical stability, but they require sintering process to address interfacial resistances.[17, 18]

Recently, halide SEs have been considered as promising alternative SEs due to their favorable combination of high ionic conductivity, wide electrochemical stability window, and chemical stability against high-voltage cathodes.[19-28] Lithium ternary chlorides, Li_3MCl_6, exhibit high ionic conductivity (0.5–3 mS/cm for Li_3MCl_6 with M = Y, Er, In, Sc, and Yb) and chemical stability against 4 V-class oxide cathode materials.[22-28] The ionic conductivity of Li_3MCl_6 (M = Y, Er, Fe, In, and Yb) was further improved by the aliovalent substitution of M^{3+} to Zr^{4+}.[28-32]

[a] Energy Storage Research Center, Korea Institute of Science and Technology, 5, Hwarang-ro 14-gil, Seongbuk-gu, Seoul 02792, Republic of Korea
[b] School of Mechanical Engineering, Korea University, 145 Anam-ro, Seongbuk-gu, Seoul 02841, South Korea
[c] Materials Science Division, Lawrence Livermore National Laboratory, Livermore, CA, 94550, USA
[d] Division of Energy & Environment Technology, KIST School, Korea University of Science and Technology, Seoul 02792, Republic of Korea
* Corresponding Authors
Electronic Supplementary Information (ESI) available: [details of any supplementary information available should be included here]. See DOI: 10.1039/x0xx00000x

Theoretical studies also revealed the high ionic conductivity of Li_3MCl_6 and $Li_{3-x}M_{1-x}Zr_xCl_6$, above 10 mS/cm and high oxidation potential of approximately 4.3 V.[33-36]

Although lithium chloride SEs, Li_3MCl_6 are considered promising candidates for high-voltage ASSBs, very few investigations of sodium chloride SEs, such as Na_3MCl_6 (M = Y and Er), Na_2ZrCl_6, and Zr-substituted $Na_{3-x}M_{1-x}Zr_xCl_6$ (M = Y and Er),[37-40] have been reported in the literature. Therefore, a systematic screening of Na_3MCl_6 with a broad variety of elements, M^{3+}, would be a fundamental guideline for developing novel sodium chloride SEs. In this study, we provided a material design strategy for sodium chloride SEs by assessing the phase stability, electrochemical stability, and transport properties of Na_3MCl_6 SEs with 26 M^{3+} elements.

Structural calculations indicated that Na_3MCl_6 exhibited the crystal structures of the $P\bar{3}1c$, $P2_1/n$, and $R\bar{3}$ phases, and the stable phase of Na_3MCl_6 was dependent on the type and ionic radius of M. Na_3MCl_6 typically exhibited a high oxidation potential, demonstrating good electrochemical stability at high voltages. The Na-ion migration pathways and migration energy barriers in Na_3MCl_6 from the bond-valence site energy (BVSE) method indicated that Na-ion migration in monoclinic $P2_1/n$ and trigonal $R\bar{3}$ phases was slower than that in the trigonal $P\bar{3}1c$ phase. *Ab initio* molecular dynamics (AIMD) simulations further revealed that Na_3CrCl_6 ($P\bar{3}1c$ phase) had higher ionic conductivity than Na_3ErCl_6 ($P2_1/n$ phase) and Na_3GdCl_6 ($R\bar{3}$ phase). Although the $P2_1/n$ and $R\bar{3}$ phases exhibited low ionic conductivity, the aliovalent substitution of M^{3+} with Zr^{4+} significantly increased the ionic conductivity up to four orders of magnitude. Ionic substitutions in Na_3MCl_6 would be a promising approach for the enhancement of ionic transport, and the optimization of the element type and ratio of substitution can further increase the ionic conductivity of Na_3MCl_6.

Methods

First principles calculations were conducted using density functional theory (DFT) with a plane-wave basis set and the projector-augmented wave method,[41] as implemented in the Vienna *Ab initio* Simulation Package.[42, 43] The generalized gradient approximation of Perdew, Burke, and Ernzerhof was employed for the exchange-correlation energy.[44] A van der Waals density functional (vdW-DF, optB86b-vdW)[45] was used to address the interaction in layered chloride structures based on previous works.[34] An energy cutoff of 520 eV was used for the plane-wave basis, and the k-point grids were generated using the Python Materials Genomics (Pymatgen) code,[46] where the k-point densities were at least 1000/atom. The ionic positions were relaxed until the forces were less than 0.01 eV Å^{-1}, and the convergence criterion for the electronic self-consistency loop was set to 10^{-5} eV. Spin-polarized calculations were performed for the transition metals and lanthanides.

The simulation cells of Na_3MCl_6 were generated using the experimental structures of Na_3MCl_6, exhibiting trigonal $P\bar{3}1c$ (space group number, S.G., #163),[47, 48] monoclinic $P2_1/n$ (S.G. #14),[37, 38, 49] and trigonal $R\bar{3}$ (S.G. #148)[50] crystal structures. In addition, the experimental structures of lithium ternary chlorides Li_3MCl_6, including monoclinic $C2/m$ (S.G. #12)[24, 26] and trigonal $P\bar{3}m1$ (S.G. #164)[22, 35] structures were also used to generate the simulation cells of Na_3MCl_6. A total of 26 M^{3+} cations were selected for Na_3MCl_6, including 3d transition metals (Cr, V, Fe, and Ti), group 3 elements (Sc, Lu, and Y), group 13 and 15 elements (Al, Ga, In, Tl, and Bi), and lanthanides (Yb, Tm, Er, Ho, Dy, Tb, Gd, Eu, Sm, Pm, Nd, Pr, Ce, and La). For the partially occupied Na sites in the Na_3MCl_6 structures, the ionic configuration with the lowest total energy was selected for subsequent calculations.

The phase stability of Na_3MCl_6 was examined using Na-M-Cl phase diagrams in the Materials Project (MP) database.[51] Competing stable decomposition phases for Na_3MCl_6 (e.g., MCl_3, $NaMCl_4$, and NaCl) were collected to evaluate the energy above the convex hull (E_{hull}) of Na_3MCl_6. The Na_3MCl_6 phase with an E_{hull} value below 25 meV/atom was considered as the stable phase, which can be stabilized by entropic effects. The electrochemical stability window of Na_3MCl_6 was calculated using the grand potential phase diagram as a function of the chemical potential of Na:

$$\mu_{\mathrm{Na}}(\varphi) = \mu_{\mathrm{Na},0} - e\varphi \ , \tag{1}$$

where $\mu_{\mathrm{Na},0}$ is the chemical potential of Na metal, e is the elementary charge, and φ is the applied potential referenced to the Na metal anode. The Pymatgen code was used to generate the grand phase diagram and determine the electrochemical stability window. The total energies of Na_3MCl_6 were recalculated using consistent settings in the MP for the electrochemical stability calculations.

Na-ion migration pathway and its energy barrier were predicted using the BVSE method as implemented in the SoftBV software.[52] Na site energies were calculated for a dense grid with a resolution of 0.1 Å using the Morse type interaction potential. The Na-ion migration path was identified based on the isosurface of the Na site energy, whereas the minimum energy required to connect a migration path was calculated for the migration energy barrier.

Na-ion diffusivity in Na_3MCl_6 was obtained using AIMD simulations. Because AIMD simulations require significant computational effort, a lower energy cut-off of 350 eV, gamma point-only k-point grid, and the NVT ensemble with a Nosé-Hoover thermostat were employed. The mean squared displacement (MSD) was evaluated at 700, 750, 800, 900, and 1000 K for the 40–75 ps window, and the time step for all AIMD calculations was 2 fs. The diffusion coefficient, D, was calculated using the MSD of the Na ions:

$$D = \frac{1}{2dt}\left\langle\left[\mathbf{r}(t+t_0) - \mathbf{r}(t_0)\right]^2\right\rangle \tag{2}$$

where d is the dimensionality of the system, t_0 is the initial time, t is the time for MSD, and the angled brackets indicate the average overall Na ions. For the statistical reliability of the AIMD simulations, the average diffusion coefficient and its standard deviation were evaluated using three independent AIMD simulations at each temperature. The ionic conductivity of Na, σ , was calculated using the Nernst–Einstein equation:

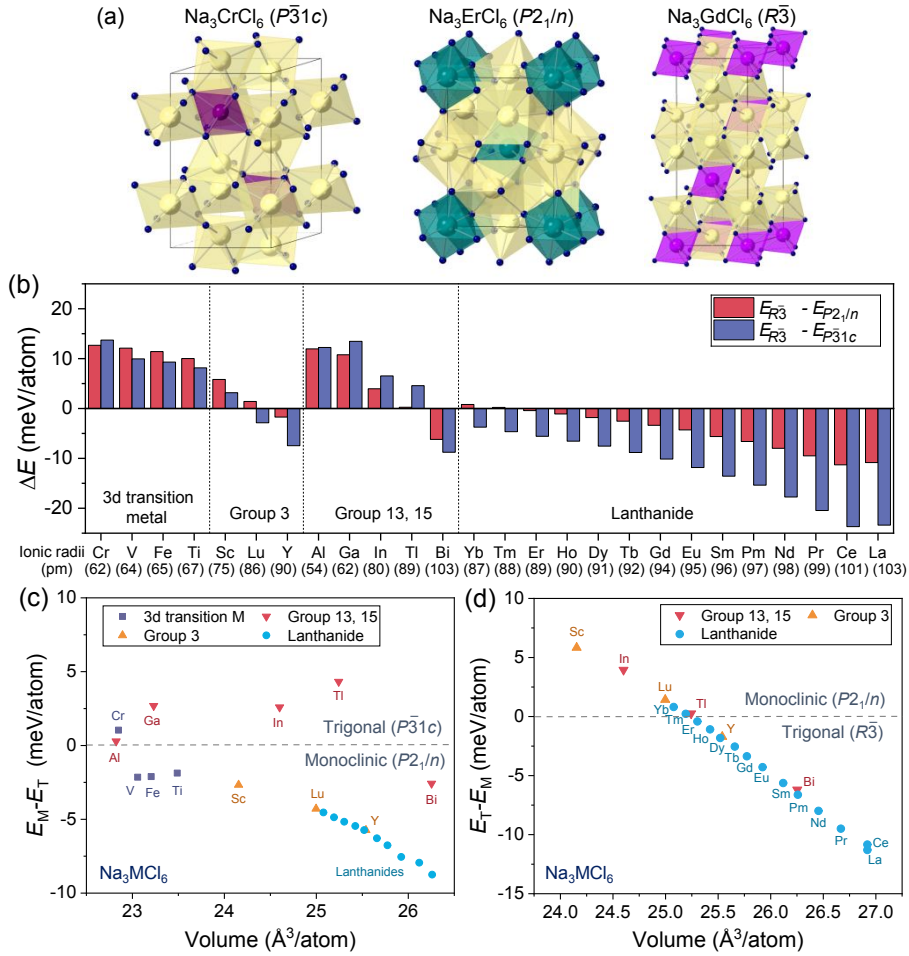

Fig. 1 (a) Crystal structures of sodium chlorides Na_3MCl_6 (M=Cr, Er, and Gd) with $NaCl_6$ polyhedra (yellow) and MCl_6 octahedra. (b-d) Structural preference of Na_3MCl_6 among the trigonal $P\bar{3}1c$, monoclinic $P2_1/n$, and trigonal $R\bar{3}$ systems. (b) Energy differences among the crystal structures of $P\bar{3}1c$, $P2_1/n$, and $R\bar{3}$, as a function of the effective ionic radii of M. (c-d) Energy difference between (c) trigonal $P\bar{3}1c$ and monoclinic $P2_1/n$, and (d) monoclinic $P2_1/n$ and trigonal $R\bar{3}$ structures of Na_3MCl_6, as a function of the volume of structures. The values in (b-d) were divided into four groups based on M: 3d transition metals, group 3 elements, group 13 and 15 elements, and lanthanides

$$\sigma = \frac{(ze)^2 cD}{k_B T} \quad (3)$$

where z is the valence of the Na ion, e is the elementary charge, c is the concentration of the Na ion, and D is the diffusion coefficient of Na ions. The ionic trajectories of Na during the AIMD simulations were recorded using a grid with dimensions of 25 × 25 × 25 to visualize Na-ion migration. Isosurfaces of the ionic probability densities were obtained with respect to the mean ionic probability density (P_0).

Results

The structure of sodium chloride Na_3MCl_6 was determined by comparing the total energy among the trigonal $P\bar{3}1c$, monoclinic $P2_1/n$, and trigonal $R\bar{3}$ phases based on the experimental structures of Na_3MCl_6. The crystal structures of the $P\bar{3}1c$, $P2_1/n$, and $R\bar{3}$ phases (from Na_3CrCl_6, Na_3ErCl_6, and Na_3GdCl_6, respectively), are presented in Figure 1(a) with $NaCl_6$ polyhedra (yellow) and MCl_6 octahedra. The structural preference of Na_3MCl_6 was evaluated by calculating the total energy differences (ΔE) between the phases (ΔE between trigonal $R\bar{3}$ and monoclinic $P2_1/n$ ($E_{R\bar{3}} - E_{P2_1/n}$) phases, and between trigonal $R\bar{3}$ and trigonal $P\bar{3}1c$ ($E_{R\bar{3}} - E_{P\bar{3}1c}$) phases), as shown in Figure 1(b). The negative values of ΔE in Figure 1(b) indicate the preference of the trigonal $R\bar{3}$ phase, whereas the positive values of ΔE demonstrate the preference of the $P\bar{3}1c$ and $P2_1/n$ phases compared to the $R\bar{3}$ phase. The values of ΔE decreased as the size of M increased, indicating that Na_3MCl_6 with relatively large M cations preferred the trigonal $R\bar{3}$ phase. The energy differences among the phases in Figure 1(b) are also presented as a function of the volume of the structures in Figure S1. The values of ΔE decreased as the volume of Na_3MCl_6 increased, suggesting a preference for the trigonal $R\bar{3}$ phase for Na_3MCl_6 with relatively large M cations. The values of ΔE and volume of Na_3MCl_6 for the $P\bar{3}1c$, $P2_1/n$, and $R\bar{3}$ phases are listed in Tables S1 and S2, respectively.

The structural preference of the monoclinic $P2_1/n$ phase compared to the trigonal $P\bar{3}1c$ and $R\bar{3}$ phases was examined using the values of ΔE, as shown in Figures 1(c) and (d), respectively. As shown in Figure 1(c), Na_3MCl_6 generally preferred the monoclinic $P2_1/n$ phase as the volume of Na_3MCl_6 increased. Na_3MCl_6 with relatively large M cations, such as group

Table 1. Stable phase, E_{hull}, and decomposition phases of Na_3MCl_6.

M	M	M_{Radii} (pm)	Na_3MCl_6	Stable phase	E_{hull} (meV/atom)	Stability	Decomp. phases
3d transition metal	Cr	61.5	Na_3CrCl_6	$P\bar{3}1c$	14	Meta-Stable	$CrCl_3$, NaCl
	V	64	Na_3VCl_6	$P2_1/n$	22	Meta-Stable	VCl_3, NaCl
	Fe	64.5	Na_3FeCl_6	$P2_1/n$	27	Unstable	$NaFeCl_4$, NaCl
	Ti	67	Na_3TiCl_6	$P2_1/n$	26	Unstable	$TiCl_3$, NaCl
Group 3	Sc	74.5	Na_3ScCl_6	$P2_1/n$	-5	Stable	N/A
	Lu	86.1	Na_3LuCl_6	$P2_1/n$	-7	Stable	N/A
	Y	90	Na_3YCl_6	$R\bar{3}$	-11	Stable	N/A
Group 13	Al	53.5	Na_3AlCl_6	$P\bar{3}1c$	22	Meta-Stable	$NaAlCl_4$, NaCl
	Ga	62	Na_3GaCl_6	$P\bar{3}1c$	41	Unstable	$NaGaCl_4$, NaCl
	In	80	Na_3InCl_6	$P\bar{3}1c$	-4	Stable	N/A
	Tl	88.5	Na_3TlCl_6	$P\bar{3}1c$	-2	Stable	N/A
Group 15	Bi	103	Na_3BiCl_6	$R\bar{3}$	-10	Stable	N/A
Lanthanide	Yb	86.8	Na_3YbCl_6	$P2_1/n$	-10	Stable	N/A
	Tm	88	Na_3TmCl_6	$P2_1/n$	-6	Stable	N/A
	Er	89	Na_3ErCl_6	$R\bar{3}$	-3	Stable	N/A
	Ho	90.1	Na_3HoCl_6	$R\bar{3}$	1	Meta-Stable	$HoCl_3$, NaCl
	Dy	91.2	Na_3DyCl_6	$R\bar{3}$	6	Meta-Stable	$DyCl_3$, NaCl
	Tb	92.3	Na_3TbCl_6	$R\bar{3}$	6	Meta-Stable	$NaTbCl_4$, NaCl
	Gd	93.5	Na_3GdCl_6	$R\bar{3}$	15	Meta-Stable	$GdCl_3$, NaCl
	Eu	94.7	Na_3EuCl_6	$R\bar{3}$	22	Meta-Stable	$EuCl_3$, NaCl
	Sm	95.8	Na_3SmCl_6	$R\bar{3}$	30	Unstable	$SmCl_3$, NaCl
	Pm	97	Na_3PmCl_6	$R\bar{3}$	36	Unstable	$PmCl_3$, NaCl
	Nd	98.3	Na_3NdCl_6	$R\bar{3}$	43	Unstable	$NdCl_3$, NaCl
	Pr	99	Na_3PrCl_6	$R\bar{3}$	50	Unstable	$PrCl_3$, NaCl
	Ce	101	Na_3CeCl_6	$R\bar{3}$	57	Unstable	$CeCl_3$, NaCl
	La	103.2	Na_3LaCl_6	$R\bar{3}$	53	Unstable	$LaCl_3$, NaCl

3 elements and lanthanides, exhibited a monoclinic $P2_1/n$ phase. Na_3MCl_6 with 3d transition metals slightly preferred the monoclinic $P2_1/n$ phase, whereas Na_3MCl_6 with a relatively small Cr preferred the trigonal $P\bar{3}1c$ phase, which was consistent with the experimental results.[48] The preference tendency of the monoclinic phase was slightly different for Na_3MCl_6 with group 13 elements (Al, Ga, In, and Tl), exhibiting trigonal $P\bar{3}1c$. The preference tendency of the trigonal $R\bar{3}$ phase compared to the monoclinic $P2_1/n$ phase for Na_3MCl_6 is illustrated in Figure 1(d). Na_3MCl_6 with relatively large M cations exhibited a trigonal $R\bar{3}$ phase, and the transition from the monoclinic to trigonal phase occurred with an ionic radius of 90 pm. The phase transition to the trigonal $R\bar{3}$ phase was consistent among the elements of groups 3, 13, and 15, and lanthanides.

The most stable phase of Na_3MCl_6 among the trigonal $P\bar{3}1c$, monoclinic $P2_1/n$, and trigonal $R\bar{3}$ phases is shown in Table 1. Na_3MCl_6 with relatively small M cations (Cr) and group 13 elements (Al, Ga, In, and Tl) preferred the trigonal $P\bar{3}1c$ phase, whereas Na_3MCl_6 with relatively large M cations (> 90 pm, Y, Bi, Er, Ho, Dy, Tb, Gd, Eu, Sm, Pm, Nd, Pr, Ce, and La) preferred the trigonal $R\bar{3}$ phase. Monoclinic $P2_1/n$ was the preferred phase of Na_3MCl_6, with M cations exhibiting moderate ionic radii, such as V, Fe, Ti, Sc, Lu, Yb, and Tm. Additionally, the stability of Na_3MCl_6 structures with monoclinic $C2/m$ or trigonal $P\bar{3}m1$ phases from the Li_3MCl_6 structures was also investigated by comparing the total energy differences among the phases. Table S3 shows the most stable phase of Na_3MCl_6 among the $P\bar{3}1c$, $P2_1/n$, and $R\bar{3}$ phases, and the energy differences of the Na_3MCl_6 phase against the $C2/m$ and $P\bar{3}m1$ phases. The positive values of ΔE indicate that the Na_3MCl_6 structures with the $C2/m$ and $P\bar{3}m1$ phases were unstable phases, compared to the Na_3MCl_6 structures based on the $P\bar{3}1c$, $P2_1/n$, and $R\bar{3}$ phases. The values of ΔE were 5–45 meV/atom, suggesting that $C2/m$ and $P\bar{3}m1$ from Li_3MCl_6 structures are unfavorable phases for Na_3MCl_6.

The phase stability of Na_3MCl_6 was determined using the E_{hull} of Na_3MCl_6 against competing decomposition phases, as shown in Table S4. The decomposition phases generally consisted of NaCl and MCl_3 (Tables S5 and S6), and $NaMCl_4$ (M = Fe, Sc, Lu, Al, Ga, Tm, and Tb) phases were also considered as stable decomposition phases. In Table 1, Na_3MCl_6 phases with E_{hull} values higher than 25 meV/atom, such as Na_3MCl_6 (M = Fe, Ti, Ga, Sm, Pm, Nd, Pr, Ce, and La) were considered as unstable phases, whereas Na_3MCl_6 phases with a positive value of E_{hull} below 25 meV/atom such as Na_3MCl_6 (M= Cr, V, Al, Ho, Dy, Tb, Gd, and Eu) were considered as metastable phases, which can be stabilized by entropic effects. Na_3MCl_6 with Sc, Lu, Y, In, Tl, Bi, Yb, Tm, and Er exhibited negative values of E_{hull} indicating that these phases were stable against the decomposition phases. The heat map in Figure 2 presents the E_{hull} of Na_3MCl_6 among the crystal structures of $P\bar{3}1c$, $P2_1/n$, $R\bar{3}$, $C2/m$, and $P\bar{3}$

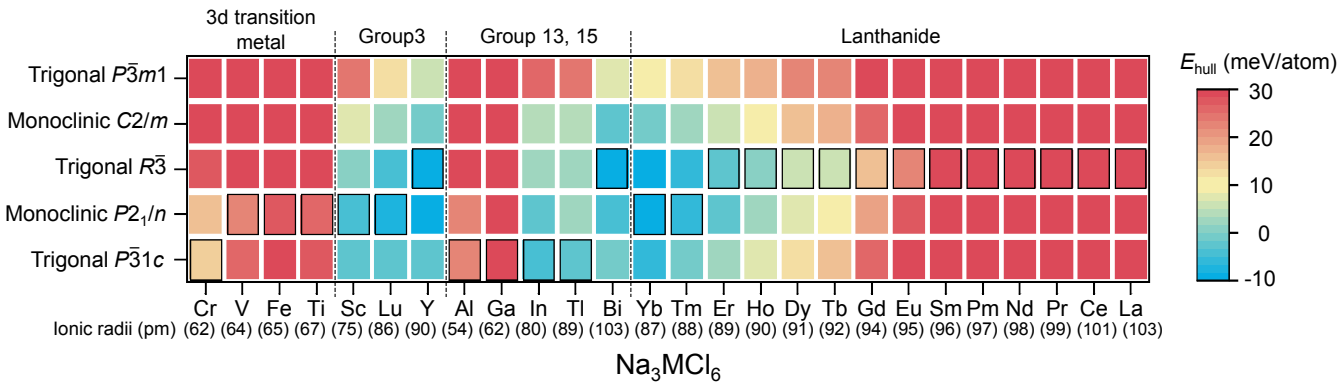

Fig. 2 Heat map of the energy above hull (E_{hull}) for sodium chlorides Na_3MCl_6 with the crystal structures of $P\bar{3}1c$, $P2_1/n$, $R\bar{3}$, $C2/m$, and $P\bar{3}m1$. The value of E_{hull} and the decomposition phases for Na_3MCl_6 are shown in Table S4. The most stable phases for each Na_3MCl_6 are indicated by a black box.

$m1$, where the most stable phase is indicated by a black box. Stable Na_3MCl_6 phases were colored with light blue, and changed to light green, yellow, orange, and red, as E_{hull} increased.

The electrochemical stability window of Na_3MCl_6 was examined using the grand potential diagram as a function of the Na chemical potential, as shown in Figure 3. The most stable phase of Na_3MCl_6 (Table 1) was used to calculate the electrochemical stability of Na_3MCl_6 against reduction and oxidation. The oxidation potential of most Na_3MCl_6 was approximately 3.8 V, suggesting good stability against oxidation. Phase decomposition by oxidation reactions occurs at a higher voltage than that from these theoretical thermodynamic calculations, owing to the kinetic barrier of the reaction and protective decomposition layers. The high oxidation potential of Na_3MCl_6 enables its use in cathodes, demonstrating a considerable advantage compared to sulfide SEs, which exhibit low oxidation potentials (e.g., 2.49 V for Na_3PS_4 and 2.35 V for Na_3SbS_4)[53]. The oxidation potential of Na_3VCl_6 was lower (2.8 V) than that of Na_3MCl_6 because of the decomposition phase of VCl_4.

The reduction potential of Na_3MCl_6 with group 3 elements and lanthanides was approximately 0.5 V, exhibiting a wide electrochemical stability window (0.5–3.8 V). The reduction potential of Na_3MCl_6 with p-block elements (M = Al, In, Tl, and Bi) and 3d transition metals (Cr and V) was higher than 1.5 V, indicating that these elements were unstable against reduction reaction in contact with anodes. These results are in agreement with those of previous studies for lithium chlorides, Li_3MCl_6, which revealed the wide electrochemical window (0.7–4.3 V) of Li_3MCl_6 with group 3 elements and lanthanides, whereas Li_3MX_6 with p-block elements (M = In, Bi, and Tl) was unstable against reduction reaction in contact with anodes.[34] Although Na_3MCl_6 with group 3 elements and lanthanides showed wide electrochemical window with low reduction potential of approximately 0.5 V, the reduction products of Na_3MCl_6 included metal M, which enable to conduct electrons, resulting in continuous reduction reactions.[54] Na_3MCl_6 also exhibited the instability against the Na metal, and reduction products included metal M, as shown in Table S7. Therefore, adequate coatings should be considered to stabilize the interface between Na_3MCl_6 and anodes.[55] The reduction and oxidation potentials of Na_3MCl_6, and their corresponding phase equilibria are listed in Table S8.

The chemical stability of Na_3MCl_6 against cathode materials was evaluated by calculating the reaction energy between Na_3MCl_6 and four cathode materials ($NaCrO_2$, $NaMnO_2$, $NaCoO_2$, and $NaNiO_2$) as shown in Figure S2. Na_3MCl_6 exhibited the reaction energy approximately 0.1 eV/atom, which was significantly lower than that of sulfide SE, Na_3PS_4. Although the negative value of reaction energy suggested the thermodynamically favorable reaction between Na_3MCl_6 and cathode materials, kinetic barrier could prevent the decomposition due to the low reaction energy, while decomposition phases at the interface could also prevent further decomposition of the bulk phase.

The Na-ion migration pathway in Na_3MCl_6 was predicted using the BVSE method, as shown in Figure 4. The Na-ion migration paths within Na_3CrCl_6 (trigonal $P\bar{3}1c$), Na_3ErCl_6 (monoclinic $P2_1/n$), and Na_3GdCl_6 (trigonal $R\bar{3}$) are illustrated in Figures 4(a), (b), and (c), respectively, using the isosurface (light blue) of the Na site energy. The trigonal $P\bar{3}1c$ and $R\bar{3}$ phases exhibited a one-dimensional migration path along the z-axis between octahedral sites (Oct.–Oct.), and three-dimensional migration paths between octahedral sites via tetrahedral interstitial sites (Oct.–Tet.–Oct.). The monoclinic $P2_1/n$ phase included the Na-ion migration path between octahedral and

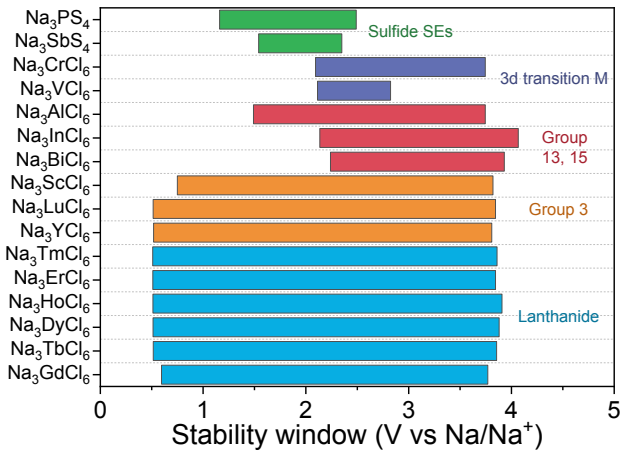

Fig. 3 Electrochemical stability window of sodium chlorides (Na_3MCl_6) and sulfide SEs (Na_3PS_4 and Na_3SbS_4).

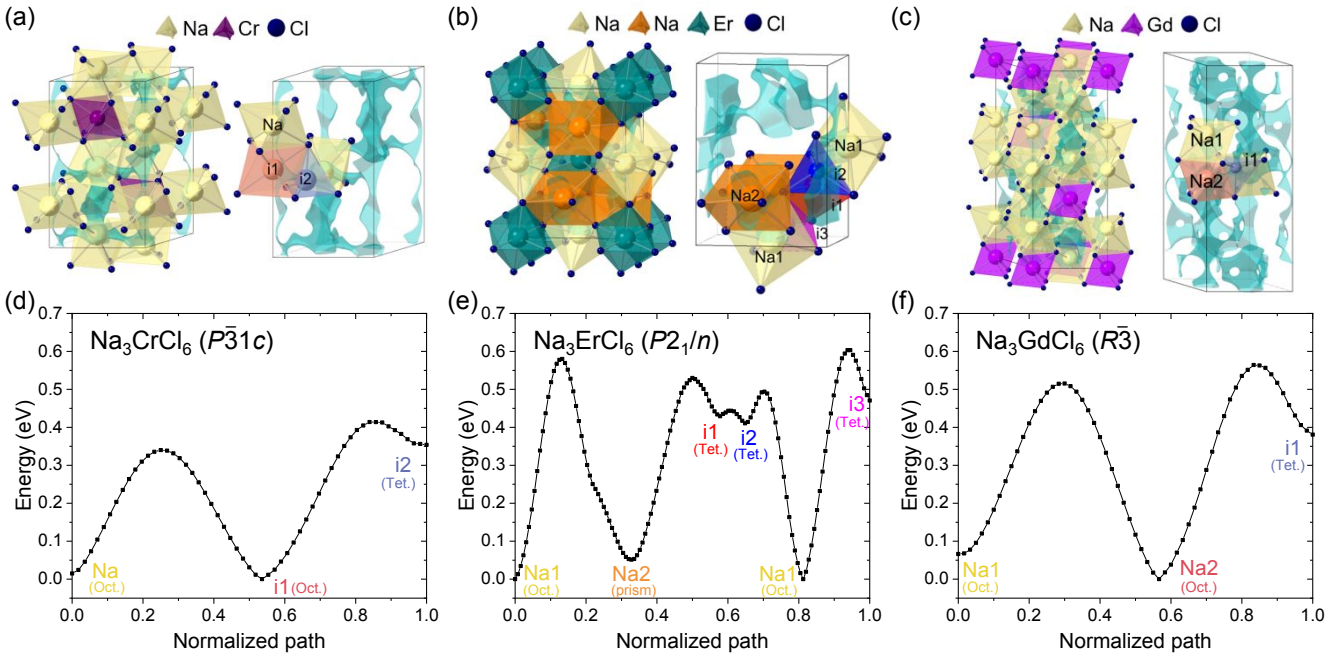

Fig. 4 Na-ion migration pathway in (a) Na_3CrCl_6 (trigonal $P\bar{3}1c$), (b) Na_3ErCl_6 (monoclinic $P2_1/n$), and (c) Na_3GdCl_6 (trigonal $R\bar{3}$) predicted by the BVSE method: (a, c) one-dimensional path between octahedral sites (Oct.–Oct.), and three-dimensional path between octahedral sites via tetrahedral interstitial sites (Oct.–Tet.–Oct.); (b) migration paths between octahedral and prism sites (Oct.–Prism), and migration paths between octahedral and prism sites via tetrahedral interstitial sites (Oct.–Tet.–Prism). Details of migration pathways are shown in Figures S3–5. (d-f) Na-ion migration energy barriers along the migration paths in (d) Na_3CrCl_6, (e) Na_3ErCl_6, and (f) Na_3GdCl_6.

prism sites (Oct.–Prism), and between octahedral and prism sites via tetrahedral interstitial sites (Oct.–Tet.–Prism), which was in good agreement with a previous study.[37] Details of Na-ion migration paths for trigonal $P\bar{3}1c$, monoclinic $P2_1/n$, and trigonal $R\bar{3}$ phases are presented in Figures S3, S4, and S5, respectively.

The energy barriers of Na-ion migration through the paths in Figures 4(a-c) were evaluated using the BVSE method, as shown in Figures 4(d-f). The energy barriers of Na-ion migration through face sharing octahedral sites (Na-i1) and octahedral sites via interstitial tetrahedral sites (i1-i2-Na) in the trigonal $P\bar{3}1c$ were 0.34 and 0.41 eV, respectively. The energy barriers of Na-ion migration in monoclinic $P2_1/n$ and trigonal $R\bar{3}$ phases were considerably higher than those in trigonal $P\bar{3}1c$. The energy barriers of migration in the monoclinic $P2_1/n$ phase were 0.58 eV for the direct migration path between octahedral and prism sites (Na1-Na2), 0.49 eV for the migration path between octahedral and prism sites via two tetrahedral interstitial sites (Na2-i1-i2-Na1), and 0.60 eV for the migration path between octahedral and prism sites via tetrahedral interstitial sites (Na1-i3-Na2). The trigonal $R\bar{3}$ phase exhibited the energy barriers of 0.52 for the migration path through face sharing octahedral sites (Na1-Na2) and 0.56 eV for octahedral sites via interstitial tetrahedral site (Na1-i1-Na2). Based on the values of the energy barrier, the Na-ion diffusivity in the trigonal $P\bar{3}1c$ phase would be higher than that in the monoclinic $P2_1/n$ and trigonal $R\bar{3}$ phases. As the BVSE method is a simplified empirical energy calculation that often underestimates or overestimates the activation energy,[33, 56] the relative height of the migration barrier among the three phases was emphasized in this study. Na-ion migration in Na_3MCl_6 was further investigated using AIMD calculations.

The Na-ion diffusivity in Na_3MCl_6 (M = Cr, Er, and Gd) was calculated using the MSD derived from the AIMD simulations. Na_3ErCl_6 and Na_3GdCl_6 exhibited negligible values of Na-ion MSD (~1 Å) during 100 ps at 1000 K (Figure S6), indicating the poor ionic conductivity of Na_3ErCl_6 and Na_3GdCl_6. Earlier theoretical studies for non-conductive materials suggested that the ionic conductivity was assumed as approximately 10^{-9} S/cm at room temperature, when inter-site hopping was not found in the MSD plot at 900 K.[57] Based on the low values of Na-ion MSD for Na_3ErCl_6 and Na_3GdCl_6, the diffusion barriers for these materials would exhibit 0.5 eV or higher values.[57] Using these upper bound values, the ionic conductivities at room temperature were estimated by the extrapolation of Arrhenius relation, resulting in 2×10^{-8} S/cm for Na_3GdCl_6 and Na_3ErCl_6. When the experimental activation energy of Na_3ErCl_6 (0.65 eV) was used for the calculation,[37] the ionic conductivity was estimated to be 3×10^{-10} S/cm, which is in good agreement with the experimental ionic conductivity of 10^{-9} S/cm.[37] In contrast, the Na-ion MSD was improved in Na_3CrCl_6, as shown in Figure S7, indicating a higher Na-ion diffusivity of the trigonal $P\bar{3}1c$ phase compared to the monoclinic $P2_1/n$ and trigonal $R\bar{3}$ phases. These results are in good agreement with the energy barrier calculations obtained using the BVSE method, as shown in Figure 4. The Arrhenius plot of Na-ion diffusivity in Figure 5 indicates an activation energy of 0.57 eV for Na_3CrCl_6, resulting in an ionic conductivity of 2×10^{-7} S/cm at room temperature.

Based on the relatively low ionic conductivities of Na_3MCl_6, an additional material design strategy should be applied to improve the ionic conductivity of Na_3MCl_6. One meaningful approach to increase the ionic conductivity is the formation of Na vacancies in Na_3MCl_6 by the aliovalent substitution of M^{3+}

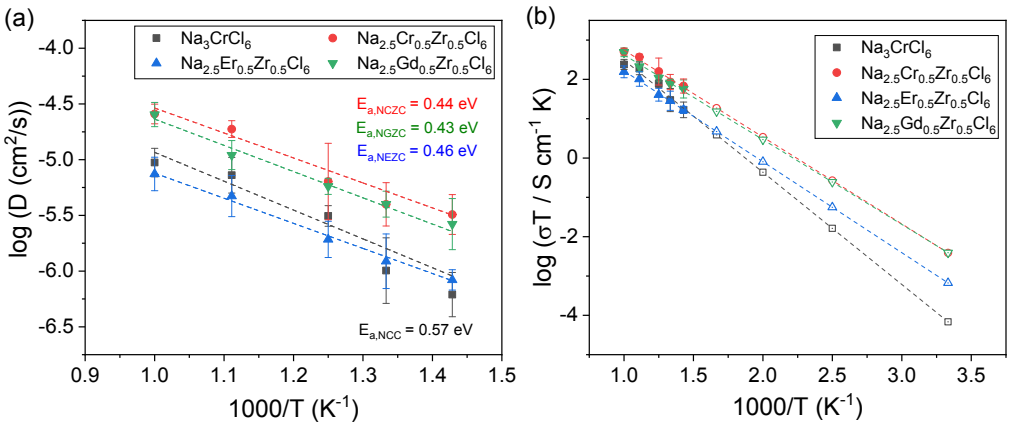

Fig. 5 Arrhenius plots of Na-ion (a) diffusivity and (b) conductivity for Na_3CrCl_6, $Na_{2.5}Cr_{0.5}Zr_{0.5}Cl_6$ (NCZC), $Na_{2.5}Er_{0.5}Zr_{0.5}Cl_6$ (NEZC), $Na_{2.5}Gd_{0.5}Zr_{0.5}Cl_6$ (NGZC). The open symbols in (b) denote the ionic conductivities obtained using the extrapolation of the Arrhenius plots for high temperature data.

with Zr^{4+}, which resulted in an increase of the ionic conductivity of Na_3ErCl_6 (10^{-9} S/cm) by approximately four orders of magnitude compared to that of $Na_{2.4}Er_{0.4}Zr_{0.6}Cl_6$ (4×10^{-5} S/cm).[37] The phase stability of Zr-substituted Na_3MCl_6 ($Na_{3-x}M_{1-x}Zr_xCl_6$) was determined as a function of the substitution levels (x= 0, 0.25, 0.5, 0.75, and 1), as listed in Table S9. All the Zr-substituted phases, $Na_{3-x}M_{1-x}Zr_xCl_6$ (M= Cr, Er, and Gd), were considered as stable compounds (E_{hull} < 25 meV) against competing decomposition phases NaCl, MCl_3, and $ZrCl_4$. Zr-substitution in Na_3MCl_6 (M= Er and Gd) increased the reduction potential to 1.7 V (Table S10), while the effect of Zr substitution on the oxidation potential of Na_3MCl_6 was negligible.

The Arrhenius plots of the Na-ion diffusivities of $Na_{2.5}M_{0.5}Zr_{0.5}Cl_6$ were obtained using AIMD calculations, as shown in Figure 5 for $Na_{2.5}Cr_{0.5}Zr_{0.5}Cl_6$ (NCZC), $Na_{2.5}Er_{0.5}Zr_{0.5}Cl_6$ (NEZC), and $Na_{2.5}Gd_{0.5}Zr_{0.5}Cl_6$ (NGZC). The activation energy of $Na_{2.5}M_{0.5}Zr_{0.5}Cl_6$ was 0.44, 0.46, and 0.43 eV for NCZC, NEZC, and NGZC, respectively, suggesting that aliovalent substitution is a promising method to enhance the ionic diffusion in Na_3MCl_6. The predicted Na-ion conductivities at room temperature were 1.3×10^{-5}, 2.2×10^{-6}, and 1.3×10^{-5} S/cm for NCZC, NEZC, and NGZC, respectively, exhibiting ionic conductivities up to four orders of magnitude higher than that in the pristine Na_3MCl_6. The predicted ionic conductivities of Zr-substituted Na_3MCl_6 phases (approximately 10^{-5} S/cm) are comparable to the highest ionic conductivity among the reported Na chloride SEs.[37-39]

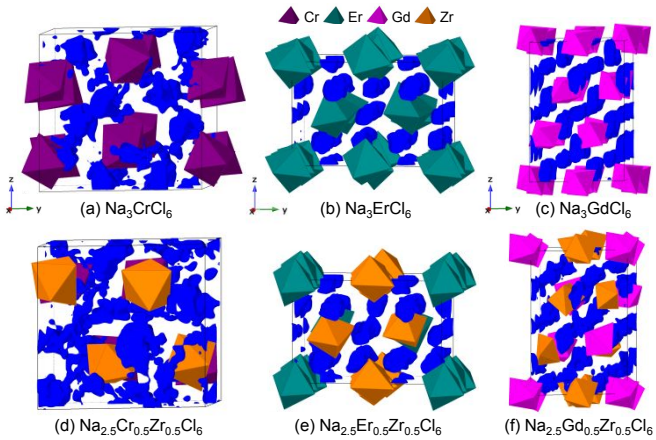

Fig. 6 Isosurfaces of the Na-ion probability densities (blue) from 40-ps AIMD calculations at 1000 K plotted using an isosurface value of $4P_0$ for (a) Na_3CrCl_6, (b) Na_3ErCl_6, (c) Na_3GdCl_6, (d) $Na_{2.5}Cr_{0.5}Zr_{0.5}Cl_6$, (e) $Na_{2.5}Er_{0.5}Zr_{0.5}Cl_6$, and (f) $Na_{2.5}Gd_{0.5}Zr_{0.5}Cl_6$. The purple, cyan-green, magenta, and orange colors correspond to Cr, Er, Gd, and Zr octahedra, respectively.

Na-ion trajectories were obtained to visualize Na-ion diffusion in Na_3MCl_6 and $Na_{2.5}M_{0.5}Zr_{0.5}Cl_6$, as shown in Figure 6. The isosurfaces of the Na-ion probability densities during 40 ps AIMD calculations at 1000 K were plotted using an isosurface value of $4P_0$. Na-ion isosurfaces for Na_3ErCl_6 and Na_3GdCl_6 exhibited localized displacements, confirming the lower Na-ion mobility in Na_3ErCl_6 and Na_3GdCl_6. Na-ion isosurfaces were more connected through the migration path in Na_3CrCl_6 compared to that in Na_3ErCl_6 and Na_3GdCl_6, which was consistent with the higher diffusivity of Na_3CrCl_6. Na-ion paths were improved in $Na_{3-x}M_{1-x}Zr_xCl_6$, indicating that Na vacancies by the aliovalent substitution facilitated Na-ion diffusion. The difference in size between the M and Zr octahedra also led to the disorder of the diffusion path, increasing the Na-ion mobility. Based on the improvement of ionic mobility by ionic substitutions, the optimization of defects in Na_3MCl_6 is a promising strategy for developing superionic Na chloride SEs. Na_3MCl_6 with the aliovalent substitution of Ti^{4+} and Hf^{4+} also exhibited good phase stability (E_{hull} < 30 meV) as listed in Table S11, indicating that Ti and Hf can be potential candidates for the substitution in Na_3MCl_6.

Conclusions

Halide SEs have been reported as promising alternative SEs to other types of SEs owing to their high ionic conductivity and wide electrochemical stability window. In this study, systematic assessments of the phase stability, electrochemical stability, and transport properties of Na_3MCl_6 were performed to provide design insights for sodium chloride SEs. Structural calculations revealed that sodium chloride Na_3MCl_6 exhibited the crystal structures of the $P\bar{3}1c$, $P2_1/n$, and $R\bar{3}$ phases, and that the phase preference was dependent on the types and ionic radii of M. Na_3MCl_6 with relatively small M cations and group 13 elements preferred the trigonal $P\bar{3}1c$ phase, whereas Na_3MCl_6 with

moderate ionic radii preferred the monoclinic $P2_1/n$ phase. Na_3MCl_6 generally showed a preference for the trigonal $R\bar{3}$ phase with relatively large M cations above 90 pm. Phase stability calculations indicated that Na_3MCl_6 (M = Cr, V, Sc, Lu, Y, Al, In, Tl, Bi, Yb, Tm, Er, Ho, Dy, Tb, Gd, and Eu) can be considered as stable structures. Na_3MCl_6 typically exhibits a high oxidation potential, demonstrating considerable advantages compared to sulfide SEs. The electrochemical stability window was wide (0.5–3.8 V) for Na_3MCl_6 with group 3 elements and lanthanides, whereas the reduction potential of Na_3MCl_6 with p-block elements and 3d transition metals was higher than 1.5 V. The Na-ion migration pathway and energy barriers in Na_3MCl_6 were predicted using the BVSE method. The energy barriers in the monoclinic $P2_1/n$ and trigonal $R\bar{3}$ phases were higher than those in the trigonal $P\bar{3}1c$ phase. AIMD simulations were performed to examine Na-ion diffusion in Na_3MCl_6. Na_3CrCl_6 had a higher ionic conductivity than Na_3ErCl_6 and Na_3GdCl_6, but all Na_3MCl_6 phases exhibited low ionic conductivity. The aliovalent substitution of M^{3+} with Zr^{4+} increased the ionic conductivity up to four orders of magnitude compared to that of the pristine phase, suggesting that Na vacancy formation in Na_3MCl_6 is a crucial approach to improve the ionic conductivity.

Conflicts of interest

There are no conflicts to declare.

Acknowledgements

This work was supported by the Technology Development Program to Solve Climate Changes of the National Research Foundation (NRF) funded by the Ministry of Science & ICT of Korea (2017M1A2A2044482); by the Development Program of Core Industrial Technology funded by the Ministry of Trade, Industry & Energy of Korea (No. 20012318); and by the institutional program of the Korea Institute of Science and Technology (Project No. 2E30992). The work by K.K. and B.W. was performed under the auspices of the U.S. Department of Energy by Lawrence Livermore National Laboratory under Contract Number DE-AC52-07NA27344. B.W. acknowledges additional support from the Vehicle Technologies Office, Office of Energy Efficiency and Renewable Energy, U.S. Department of Energy.

References

1. D. Larcher and J. M. Tarascon, *Nature Chemistry*, 2015, **7**, 19-29.
2. P. Albertus, S. Babinec, S. Litzelman and A. Newman, *Nature Energy*, 2018, **3**, 16-21.
3. J. B. Goodenough and Y. Kim, *Chemistry of Materials*, 2010, **22**, 587-603.
4. W. Hou, X. Guo, X. Shen, K. Amine, H. Yu and J. Lu, *Nano Energy*, 2018, **52**, 279-291.
5. Y. Lu, L. Li, Q. Zhang, Z. Niu and J. Chen, *Joule*, 2018, **2**, 1747-1770.
6. Y. Wang, S. Song, C. Xu, N. Hu, J. Molenda and L. Lu, *Nano Materials Science*, 2019, **1**, 91-100.
7. T. Krauskopf, C. Pompe, M. A. Kraft and W. G. Zeier, *Chemistry of Materials*, 2017, **29**, 8859-8869.
8. A. Banerjee, K. H. Park, J. W. Heo, Y. J. Nam, C. K. Moon, S. M. Oh, S.-T. Hong and Y. S. Jung, *Angewandte Chemie International Edition*, 2016, **55**, 9634-9638.
9. A. Hayashi, N. Masuzawa, S. Yubuchi, F. Tsuji, C. Hotehama, A. Sakuda and M. Tatsumisago, *Nature Communications*, 2019, **10**, 5266.
10. Z. Zhang, E. Ramos, F. Lalère, A. Assoud, K. Kaup, P. Hartman and L. F. Nazar, *Energy & Environmental Science*, 2018, **11**, 87-93.
11. J.-J. Kim, K. Yoon, I. Park and K. Kang, *Small Methods*, 2017, **1**, 1700219.
12. T. Fuchs, S. P. Culver, P. Till and W. G. Zeier, *ACS Energy Letters*, 2020, **5**, 146-151.
13. H. Park, S. Yu and D. J. Siegel, *ACS Energy Letters*, 2021, **6**, 150-157.
14. Y. Xiao, Y. Wang, S.-H. Bo, J. C. Kim, L. J. Miara and G. Ceder, *Nature Reviews Materials*, 2020, **5**, 105-126.
15. H. Muramatsu, A. Hayashi, T. Ohtomo, S. Hama and M. Tatsumisago, *Solid State Ion.*, 2011, **182**, 116-119.
16. Y. Lee, J. Jeong, H.-D. Lim, S.-O. Kim, H.-G. Jung, K. Y. Chung and S. Yu, *ACS Sustainable Chemistry & Engineering*, 2021, **9**, 120-128.
17. N. Anantharamulu, K. Koteswara Rao, G. Rambabu, B. Vijaya Kumar, V. Radha and M. Vithal, *Journal of Materials Science*, 2011, **46**, 2821-2837.
18. M.-C. Bay, M. Wang, R. Grissa, M. V. F. Heinz, J. Sakamoto and C. Battaglia, *Advanced Energy Materials*, 2020, **10**, 1902899.
19. J. Liang, X. Li, K. R. Adair and X. Sun, *Accounts of Chemical Research*, 2021, **54**, 1023-1033.
20. S. Zhang, F. Zhao, S. Wang, J. Liang, J. Wang, C. Wang, H. Zhang, K. Adair, W. Li, M. Li, H. Duan, Y. Zhao, R. Yu, R. Li, H. Huang, L. Zhang, S. Zhao, S. Lu, T.-K. Sham, Y. Mo and X. Sun, *Advanced Energy Materials*, 2021, **n/a**, 2100836.
21. X. Li, J. Liang, X. Yang, K. R. Adair, C. Wang, F. Zhao and X. Sun, *Energy & Environmental Science*, 2020, **13**, 1429-1461.
22. T. Asano, A. Sakai, S. Ouchi, M. Sakaida, A. Miyazaki and S. Hasegawa, *Advanced Materials*, 2018, **30**, 1803075.
23. R. Schlem, S. Muy, N. Prinz, A. Banik, Y. Shao-Horn, M. Zobel and W. G. Zeier, *Advanced Energy Materials*, 2020, **10**, 1903719.
24. X. Li, J. Liang, J. Luo, M. Norouzi Banis, C. Wang, W. Li, S. Deng, C. Yu, F. Zhao, Y. Hu, T.-K. Sham, L. Zhang, S. Zhao, S. Lu, H. Huang, R. Li, K. R. Adair and X. Sun, *Energy & Environmental Science*, 2019, **12**, 2665-2671.
25. X. Li, J. Liang, N. Chen, J. Luo, K. R. Adair, C. Wang, M. N. Banis, T.-K. Sham, L. Zhang, S. Zhao, S. Lu, H. Huang, R. Li and X. Sun, *Angewandte Chemie International Edition*, 2019, **58**, 16427-16432.
26. J. Liang, X. Li, S. Wang, K. R. Adair, W. Li, Y. Zhao, C. Wang, Y. Hu, L. Zhang, S. Zhao, S. Lu, H. Huang, R. Li, Y. Mo and X. Sun, *Journal of the American Chemical Society*, 2020, **142**, 7012-7022.
27. L. Zhou, C. Y. Kwok, A. Shyamsunder, Q. Zhang, X. Wu and L. F. Nazar, *Energy & Environmental Science*, 2020, **13**, 2056-2063.
28. J. Park, D. Han, H. Kwak, Y. Han, Y. J. Choi, K.-W. Nam and Y. S. Jung, *Chemical Engineering Journal*, 2021, **425**, 130630.

29. K.-H. Park, K. Kaup, A. Assoud, Q. Zhang, X. Wu and L. F. Nazar, *ACS Energy Letters*, 2020, **5**, 533-539.
30. H. Kwak, D. Han, J. Lyoo, J. Park, S. H. Jung, Y. Han, G. Kwon, H. Kim, S.-T. Hong, K.-W. Nam and Y. S. Jung, *Advanced Energy Materials*, 2021, **11**, 2003190.
31. B. Helm, R. Schlem, B. Wankmiller, A. Banik, A. Gautam, J. Ruhl, C. Li, M. R. Hansen and W. G. Zeier, *Chemistry of Materials*, 2021, **33**, 4773-4782.
32. S. Y. Kim, K. Kaup, K.-H. Park, A. Assoud, L. Zhou, J. Liu, X. Wu and L. F. Nazar, *ACS Materials Letters*, 2021, **3**, 930-938.
33. D. Park, H. Park, Y. Lee, S.-O. Kim, H.-G. Jung, K. Y. Chung, J. H. Shim and S. Yu, *ACS Applied Materials & Interfaces*, 2020, **12**, 34806-34814.
34. K. Kim, D. Park, H.-G. Jung, K. Y. Chung, J. H. Shim, B. C. Wood and S. Yu, *Chemistry of Materials*, 2021, **33**, 3669-3677.
35. S. Wang, Q. Bai, A. M. Nolan, Y. Liu, S. Gong, Q. Sun and Y. Mo, *Angewandte Chemie International Edition*, 2019, **58**, 8039-8043.
36. Y. Liu, S. Wang, A. M. Nolan, C. Ling and Y. Mo, *Advanced Energy Materials*, 2020, **10**, 2002356.
37. R. Schlem, A. Banik, M. Eckardt, M. Zobel and W. G. Zeier, *ACS Applied Energy Materials*, 2020, **3**, 10164-10173.
38. E. A. Wu, S. Banerjee, H. Tang, P. M. Richardson, J.-M. Doux, J. Qi, Z. Zhu, A. Grenier, Y. Li, E. Zhao, G. Deysher, E. Sebti, H. Nguyen, R. Stephens, G. Verbist, K. W. Chapman, R. J. Clément, A. Banerjee, Y. S. Meng and S. P. Ong, *Nature Communications*, 2021, **12**, 1256.
39. H. Kwak, J. Lyoo, J. Park, Y. Han, R. Asakura, A. Remhof, C. Battaglia, H. Kim, S.-T. Hong and Y. S. Jung, *Energy Storage Materials*, 2021, **37**, 47-54.
40. Y. Qie, S. Wang, S. Fu, H. Xie, Q. Sun and P. Jena, *The Journal of Physical Chemistry Letters*, 2020, **11**, 3376-3383.
41. P. E. Blöchl, *Physical Review B*, 1994, **50**, 17953-17979.
42. G. Kresse and J. Furthmüller, *Physical Review B*, 1996, **54**, 11169-11186.
43. G. Kresse and D. Joubert, *Physical Review B*, 1999, **59**, 1758-1775.
44. J. P. Perdew, K. Burke and M. Ernzerhof, *Physical Review Letters*, 1996, **77**, 3865-3868.
45. J. Klimeš, D. R. Bowler and A. Michaelides, *Journal of Physics: Condensed Matter*, 2009, **22**, 022201.
46. S. P. Ong, W. D. Richards, A. Jain, G. Hautier, M. Kocher, S. Cholia, D. Gunter, V. L. Chevrier, K. A. Persson and G. Ceder, *Computational Materials Science*, 2013, **68**, 314-319.
47. G. Friedrich, H. Fink and H. J. Seifert, *Zeitschrift für anorganische und allgemeine Chemie*, 1987, **548**, 141-150.
48. M. Beran and G. Meyer, *Crystals*, 2011, **1**.
49. G. Meyer, S. Peter Ax, T. Schleid and M. Irmler, *Zeitschrift für anorganische und allgemeine Chemie*, 1987, **554**, 25-33.
50. G. Meyer, *Zeitschrift für anorganische und allgemeine Chemie*, 1984, **517**, 191-197.
51. A. Jain, S. P. Ong, G. Hautier, W. Chen, W. D. Richards, S. Dacek, S. Cholia, D. Gunter, D. Skinner, G. Ceder and K. A. Persson, *APL Materials*, 2013, **1**, 011002.
52. H. Chen, L. L. Wong and S. Adams, *Acta Crystallographica Section B*, 2019, **75**, 18-33.
53. H. Tang, Z. Deng, Z. Lin, Z. Wang, I.-H. Chu, C. Chen, Z. Zhu, C. Zheng and S. P. Ong, *Chemistry of Materials*, 2018, **30**, 163-173.
54. L. M. Riegger, R. Schlem, J. Sann, W. G. Zeier and J. Janek, *Angewandte Chemie International Edition*, 2021, **60**, 6718-6723.
55. S. Yu, H. Park and D. J. Siegel, *ACS Applied Materials & Interfaces*, 2019, **11**, 36607-36615.
56. R. Xiao, H. Li and L. Chen, *Scientific Reports*, 2015, **5**, 14227.
57. A. D. Sendek, E. D. Cubuk, E. R. Antoniuk, G. Cheon, Y. Cui and E. J. Reed, *Chemistry of Materials*, 2019, **31**, 342-352.

